Applied Catalysis B: Environmental 244 (2019) 620–627

Contents lists available at ScienceDirect

Applied Catalysis B: Environmental

journal homepage: www.elsevier.com/locate/apcatb

Bimetallic $Ni_{2-x}Co_xP$/N-doped carbon nanofibers: Solid-solution-alloy engineering toward efficient hydrogen evolution

Qijie Mo[a], Wenbiao Zhang[a], Liuqing He[a], Xiang Yu[a,b], Qingsheng Gao[a,*]

[a] Department of Chemistry, Jinan University, Guangzhou, 510632, China
[b] Analytic and Testing Centre, Jinan University, Guangzhou, 510632, China

ARTICLE INFO

Keywords:
Hydrogen evolution reaction
Metal phosphides
Solid-Solution alloy
Electronic modulation
Hydrogen binding energy

ABSTRACT

Exploring noble-metal-free electrocatalysts for hydrogen evolution reaction (HER) is the key issue in hydrogen economy blueprint. Herein, bimetallic $Ni_{2-x}Co_xP$ supported by N-doped carbon nanofibers (denoted as $Ni_{2-x}Co_xP$/N-C NFs) are developed via electrospinning followed by pyrolysis under an inert flow. The space confinement by *in-situ* formed N-doped carbon matrix produces ultrafine $Ni_{2-x}Co_xP$ with abundant active-sites. More importantly, the engineering on $Ni_{2-x}Co_xP$ solid-solution-alloys can vary electronic configuration and consequently optimize hydrogen binding on electrocatalyst surface, accomplishing prominent HER activity in a wide pH range. The optimal $Ni_{2-x}Co_xP$/N-C NFs afford low overpotentials (η_{10}) of 100, 130 and 110 mV to reach a current density of -10 mA cm^{-2} in 0.5 M H_2SO_4, 1.0 KOH and 1.0 M PBS (phosphate buffer saline), respectively, performing among the best of noble-metal-free electrocatalysts. With a good functionality for oxygen evolution (η_{10} = 280 mV), such composite further delivers a high efficiency for overall water splitting, featuring a comparable cell voltage (1.56 V @ 10 mA cm^{-2}) to a commercial IrO_2/C − Pt/C couple, and remarkably better stability. Identifying electrocatalysis relying on solid-solution alloys, this work will inspire the exploration of cost-efficient electrocatalysts and the new understanding on catalytic mechanisms.

1. Introduction

Sustainable and clean alternative energy have attracted wide interests due to the increasing environmental and energy crisis [1,2]. As one of the candidates, hydrogen (H_2) features its renewability, environmental-friendliness and high energy density [3]. To produce H_2 in an sustainable and efficient manner, water electrolysis using reneable electrotrical energy is promising, but suffers from inevitable dynamic overpotentials associated with hydrogen and oxygen evolution reactions (HER and OER) [4]. Electrocatalysts are necessary to decrease the overpotentials [5]. So far, the state-of-the-art electrocatalysts are platinum-based materials for HER and iridium and ruthenium oxides for OER [6,7]. However, they are severely impeded by the high cost and low earth-abundance [8].

Transition metal phosphides (TMPs) are a promising class of noble-metal-free electrocatalysts for water electrolysis [9–12]. Electrocatalysis on their surface is structure-sensitive, and thereby demands active-sites with well-defined structural and electronic configurations [13–17]. However, the necessary engineering on TMPs is highly challenging due to the easy deactivation (coarsening, phase transformation, etc.) during the preparation at extremely high temperature [18]. Efforts have been accordingly made to confine the growth of TMPs within carbon matrix, leading to well-exposed active-sites on ultrafine nanocrystals and facilitated mass transportation in porous and conducting frameworks [19]. Moreover, electronic modulation on TMPs surface is desired to overcome the weak binding with hydrogen intermediates (H*) in view of the HER kinetics [20]. To this end, bimetallic phosphides, most in form of solid-solution-alloys [20,21], highlight their facile electronic modulation via tuning composition or heteroatom doping [22].

Herein, we develop bimetallic $Ni_{2-x}Co_xP$ nanoparticles supported by N-doped carbon nanofibers (denoted as $Ni_{2-x}Co_xP$/N-C NFs) as efficient electrocatalysts, via facile electrospinning procedures followed by pyrolysis (Scheme 1). The designed NFs feature the ultrafine $Ni_{2-x}Co_xP$ (4.8 ± 0.5 nm) evenly integrated with conducting and nanoporous N-C matrix, and the one-dimensional (1D) hierarchical nanostructures that fully expose active-sites in radial direction and facilitate charge transfer along axial dimension in micron [23]. More importantly, the $Ni_{2-x}Co_xP$ solid-solution alloy can be easily tailored to fulfil electronic modulation on active-sites, as indicated by experimental and theoretical investigations. Increasing x in $Ni_{2-x}Co_xP$ leads to obviously up-shifting *d*-band center toward the Fermi level (E_F), and consequently enhances

* Corresponding author at: Department of Chemistry, Jinan University, No. 601 Huangpu Avenue West, 510632, Guangzhou, China.
E-mail address: tqsgao@jnu.edu.cn (Q. Gao).

https://doi.org/10.1016/j.apcatb.2018.11.083
Received 19 September 2018; Received in revised form 26 November 2018; Accepted 28 November 2018
Available online 29 November 2018
0926-3373/ © 2018 Elsevier B.V. All rights reserved.

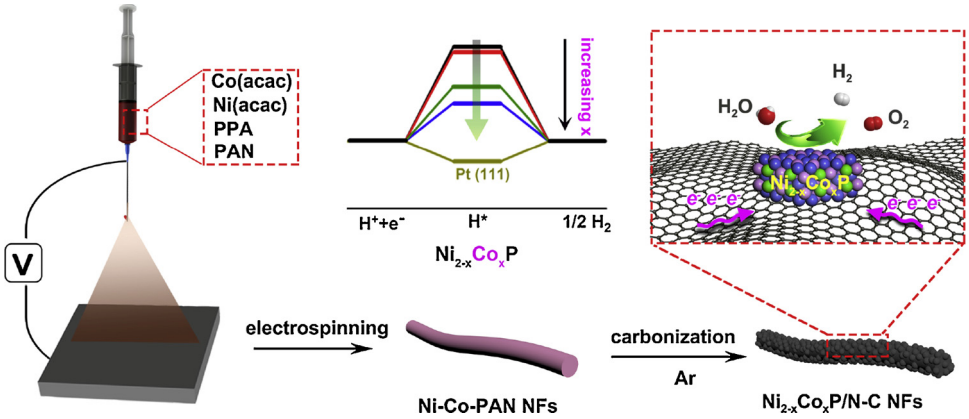

Scheme 1. Schematic illustration for the fabrication of $Ni_{2-x}Co_xP$/N-C NFs.

hydrogen binding (H-binding) on $Ni_{0.67}Co_{1.33}P$ surface. As expected, the optimal $Ni_{0.67}Co_{1.33}P$/N-C NFs afford prominent HER performance, with a low η_{10} (overpotential required to reach a current density of -10 mA cm^{-2}) of 100, 130 and 110 mV in 0.5 M H_2SO_4, 1.0 KOH and 1.0 M phosphate buffer saline (PBS), respectively. Meanwhile, they are also active for OER (η_{10} = 280 mV) in 1.0 KOH. Thereby, the bi-functional $Ni_{0.67}Co_{1.33}P$/N-C NFs accomplish a high efficiency for overall water splitting in 1.0 M KOH, with a comparable cell voltage (1.56 V @ 10 mA cm^{-2}) to commercial IrO_2/C − Pt/C coupled electrocatalysts (1.50 V @ 10 mA cm^{-2}), and a remarkably better stability.

2. Experimental section

2.1. Materials

All reagents were purchased from commercial sources and in analytical or reagent grade when possible. Polyacrylonitrile (PAN, MW = 150,000) and N, N-Dimethylformamide (DMF) were purchased from Aladdin. Phenylphosphonic acid (PPA) and cobalt/nickel acetylacetonate ($Co(acac)_2$ and $Ni(acac)_2$) were purchased from Mackin. Nafion solution (5 wt% in lower aliphatic alcohols and water) was bought from Sigma-Aldrich. All aqueous solutions were prepared using ultrapure water (> 18 MΩ cm).

2.2. Catalyst preparation

Synthesis of $Ni_{2-x}Co_xP$/N-C NFs. Typically, 1.0 g of PAN was dissolved into 13 mL of DMF with stirring at room temperature for 30 min, and then 0.47 g of PPA, and a varied amount of $Co(acac)_2$ and $Ni(acac)_2$ were added, in which the feeding molar ratio of metals (Co and Ni) to P was maintained at a consistent level of 1:1. The above mixture was vigorously stirred for 12 h. The resulting homogeneous solution was transferred to a syringe in a electronspinning setup with a aluminum foil as a collector. The injection speed was set to 0.4 mL h^{-1}, the distance between the needle and the collector was 15 cm, and the voltage to initiate the electrospinning was 18 kV. Afterwards, the collected fibers were first stabilized at 250 °C for 2 h under a H_2/Ar (5 vol%) flow, and then heated to 850 °C and kept for 5 h under an Ar flow.

Synthesis of IrO_2/C. The preparation was carried out according to the previous report [24]. 0.19 g of trisodium citrate and 11.40 g of H_2IrCl_6 aqueous solution (Ir: 0.35 wt %) were blended with 50 mL of water. A NaOH solution (1 M) was added to adjust the pH of the soultion to 7.5. After heating at 95 °C for 30 min, the solution was transferred to a flask, in which 0.184 g of carbon black (Vulcan XC72R) was already loaded. And then, it was refluxed at 95 °C for 2 h in O_2 atomsphere. The collected solid was dried at 70 °C, and then heated at 300 °C for 30 min under an air flow to remove organic ligands.

2.3. Physical measurements

Scanning electronic microscopy (SEM) and transition electronic microscopy (TEM) were performed on a ZEISS ULTRA55 and a JEOL JEM 2100 F, respectively. X-ray diffraction (XRD) was collected on Bruker D8 Advance diffractometer. X-ray photoelectron spectroscopy (XPS) was conducted on a Thermo Scientific Escalab 250Xi, using C 1 s (284.6 eV) as a reference. The composition of $Ni_{2-x}Co_xP$/N-C NFs was determined by inductively coupled plasma-atomic emission spectroscopy (ICP-AES) and CHN elemental analysis. N_2 adsorption–desorption isotherms were obtained on an automatic gas-adsorption analyzer (Quantachrome AutosorbiQ-MP). Raman spectra were collected on a laser confocal Raman microspectrometer (Horiba HR800, Jobin Yvon, Ltd.), with an excitation laser wavelength of 532 nm.

2.4. Electrochemical measurements

Electrocatalysts were loaded onto GCEs and tested in 0.5 M H_2SO_4, 1.0 M KOH and 1.0 M PBS solution on a three-electrode setup. Typically, 4 mg of catalyst and 40.0 μL of Nafion solution (5 wt%) were dispersed in water/ethanol (4:1 v/v, 1 mL) by ultrasonication for at least 30 min. For the test in 1.0 M KOH, polyvinylidene fluoride (10.0 μL, 5 wt%) was further added into the above ink. Then, 5 μL of the catalyst ink was loaded onto a GCE of 3 mm diameter. Linear-sweep voltammetry (LSV) was recorded with a scan rate of 10 mV s^{-1} on an electrochemical workstation CHI760e (Shanghai Chenhua), using a saturated calomel electrode as the reference electrode and a graphite electrode as the counter electrode. For overall water splitting, $Ni_{0.67}Co_{1.33}P$/N-C NFs modified GECs were integrated as both the anode and the cathode in a two-electrode cell. Polarization curves were recorded using LSV with a scan rate of 1.0 mV s^{-1}. All potentials reported in our manuscript were referenced to a reversible hydrogen electrode (RHE) by adding a value of (0.241 + 0.059 × pH) V. Electrochemical impedance spectroscopy (EIS) was performed from 10^{-2} to 10^6 Hz with an amplitude of 5 mV. *i*R correction was manually performed for every electrode. The compensated potential was corrected by $E_{compensated} = E_{measured} - iR_s$, where R_s is the series resistance determined by EIS.

2.5. DFT calculation details

CASTEP software implemented in Materials Studios was used for the DFT calculations. The electron exchange-correlation potential was treated by the generalized gradient approximation (GGA) in the form of Perdew–Burke–Ernzerhof (PBE) functional. A kinetic energy cutoff of 340 eV was assigned to the plane-wave basis set. To achieve accurate electronic convergence, self-consistent-field (SCF) procedures were processed with a convergence criterion of 1×10^{-6} Ha on the total

energy. 2 × 2 × 1 Monkhorst-Pack grid k-points were employed for geometric optimization. The (001) surface was taken as a model to analyze the surface electronic configurations and the corresponding binding energy, because it was highly exposed in TMPs hexagonal lattices [25]. The (001) surface was obtained by cutting $Ni_{2-x}Co_xP$ bulk along [001] direction. The thickness of surface slab is chosen to be a two-layer slab of the $Ni_{2-x}Co_xP$ unit. A vacuum layer as large as 12 Å was used along the c direction normal to the surface to avoid periodic interactions. The Gibbs free-energy change (ΔG_{H^*}) of H on the $Ni_{2-x}Co_xP$ (001) is defined as $\Delta G_{H^*} = \Delta E_{H^*} + \Delta E_{ZPE} + T\Delta S$, where ΔE_{H^*} was the adsorption energy of the atomic H on the $Ni_{2-x}Co_xP$ (001) surface, and ΔE_{ZPE} was the difference in zero-point energy (ZPE) between the adsorbed hydrogen and hydrogen in the gas phase.

3. Results and discussion

3.1. Characterization of $Ni_{2-x}Co_xP$/N-C NFs

As shown in Scheme 1, fiber-like precursors (Ni-Co-PAN NFs) are at first achieved via electrospinning a DMF solution containing PPA, PAN, and cobalt/nickel acetylacetonate ($n_{Co+Ni} : n_{PPA} = 1 : 1$). After pyrolysis at 850 °C under an Ar flow, a series of $Ni_{2-x}Co_xP$/N-C NFs are obtained (Fig. S1), in which PPA is an effective P source to react with metal acetylacetonates. By varying the feeding Co/Ni ratio in starting solution, the composition of bimetallic $Ni_{2-x}Co_xP$ is easily tailored, as determined by means of ICP-AES and CHN elemental analysis (Table S1). Their XRD patterns clearly identify the consistent crystalline structure of NiCoP (JCPDS No.: 71-2336), as shown in Fig. 1a. Because of the very similar atomic radius of Co (1.16 Å) and Ni (1.15 Å), the varied x from 0.33 to 1.67 in $Ni_{2-x}Co_xP$/N-C NFs does not bring about a visible shift in the XRD patterns. Meanwhile, Raman spectra display visible bands associated with carbon D and G bands at 1350 and 1580 cm^{-1}, respectively, confirming the presence of carbon matrix (Fig. S2). The consistent value of I_G/I_D suggests the similar graphitization in presence of either Co or Ni, both of which are catalysts to generate graphitized carbon. Furthermore, N_2 sorption isotherms present the varied textural features relying on the alloy composition. As depicted in Fig. 1b, the $Ni_{0.67}Co_{1.33}P$/N-C NFs present a specific surface area of 78.9 $m^2 g^{-1}$, higher than $Ni_{1.67}Co_{0.33}P$/N-C (37.4 $m^2 g^{-1}$), $Ni_{1.00}Co_{1.00}P$/N-C (43.3 $m^2 g^{-1}$), and $Ni_{0.33}Co_{1.67}P$/N-C NFs (47.2 $m^2 g^{-1}$). Accordingly, the pore-size increases with Co content in such fibers (inset of Fig. 1b). The $Ni_{1.67}Co_{0.33}P$/N-C, $Ni_{1.00}Co_{1.00}P$/N-C and $Ni_{0.67}Co_{1.33}P$/N-C NFs present well-defined nanoporosity, with a gradually increasing pore-size of 2.0, 3.6 and 5.6 nm, respectively. By contrast, the $Ni_{0.33}Co_{1.67}P$/N-C NFs display a dispersive pore-size distribution at a wide range (8 ~ 20 nm), which possibly results from the random stacking of NFs. The high surface area and rich nanoporosity can help to promote active-site exposure and mass transport during electrocatalysis. The evolution of specific surface and pore size should be ascribed to the interactions between PAN and metal cations. The different coordination and PAN cracking behavior on Ni^{2+} and Co^{2+} will make influences on the degradation and carbonization of PAN, which is hinted by varied weight loss in the TGA profies of various Ni-Co-PAN precursors (Fig. S3).

XPS is further conducted to analyze the chemical states and electronic interactions in $Ni_{2-x}Co_xP$/N-C NFs. Fig. 1c shows the Ni $2p_{3/2}$ core level profiles that can be deconvoluted into three peaks. On the $Ni_{1.67}Co_{0.33}P$/N-C NFs (curve I), the peak at 853.9 eV is assigned to the $2p_{3/2}$ of Ni in phosphides, while that at 856.6 eV is ascribed to the surface oxides [26]. Besides, the satellite peaks for Ni is also observed. Interestingly, the Ni $2p_{3/2}$ in phosphides gradually red-shifts to lower energy with increasing Co and reaches 853.1 eV on $Ni_{0.33}Co_{1.67}P$/N-C NFs. Accordingly, the blue-shift of Co $2p_{3/2}$ is observed with increasing Co content (Fig. 1d). The Co $2p_{3/2}$ is observed at 778.2 eV on the $Ni_{1.67}Co_{0.33}P$/N-C [27], and a higher value of 779.6 eV on the $Ni_{0.33}Co_{1.67}P$/N-C. Because P in $Ni_{2-x}Co_xP$ is fixed, the varied binding energy of Co and Ni can be ascribed to the electron transfer from Co to Ni, regading the relatively high electronegativity of Ni (1.91) *vs.* Co (1.88). Meanwhile, the XPS investigation also identifies the P species bonded with Co and Ni (Fig. S4) [28], along with those with carbon and

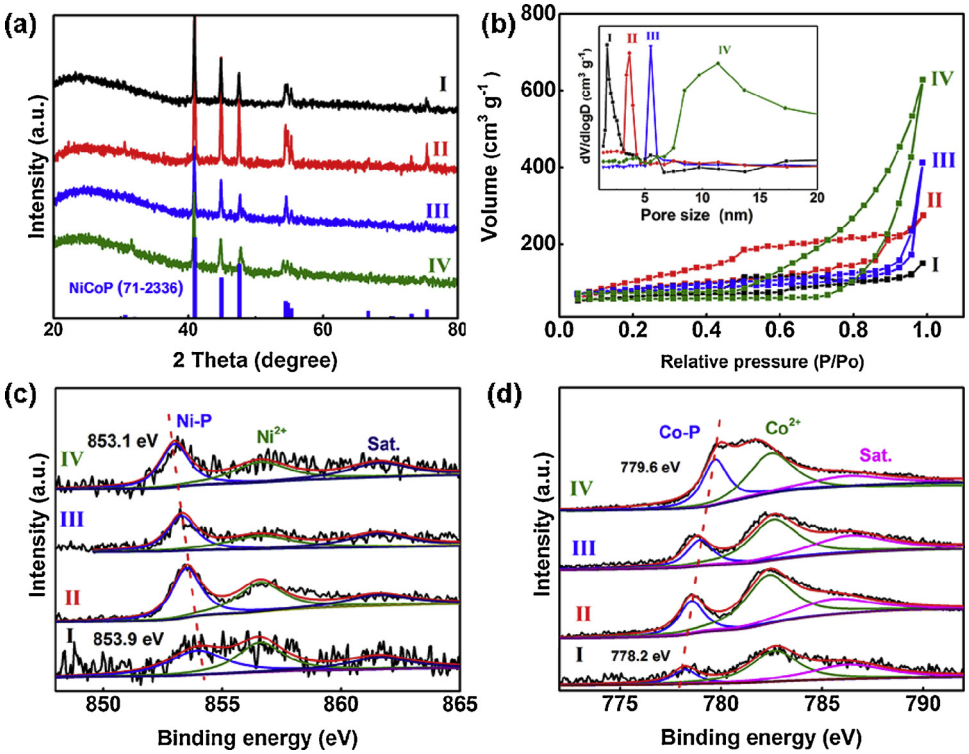

Fig. 1. (a) XRD patterns, (b) N_2 sorption isotherms, and (c) Ni $2p_{3/2}$ and (d) Co $2p_{3/2}$ XPS profiles of $Ni_{2-x}Co_xP$/N-C NFs (I: $Ni_{1.67}Co_{0.33}P$/N-C, II: $Ni_{1.00}Co_{1.00}P$/N-C, III: $Ni_{0.67}Co_{1.33}P$/N-C, IV: $Ni_{0.33}Co_{1.67}P$/N-C). Inset of b is the pore size distribution in $Ni_{2-x}Co_xP$/N-C NFs.

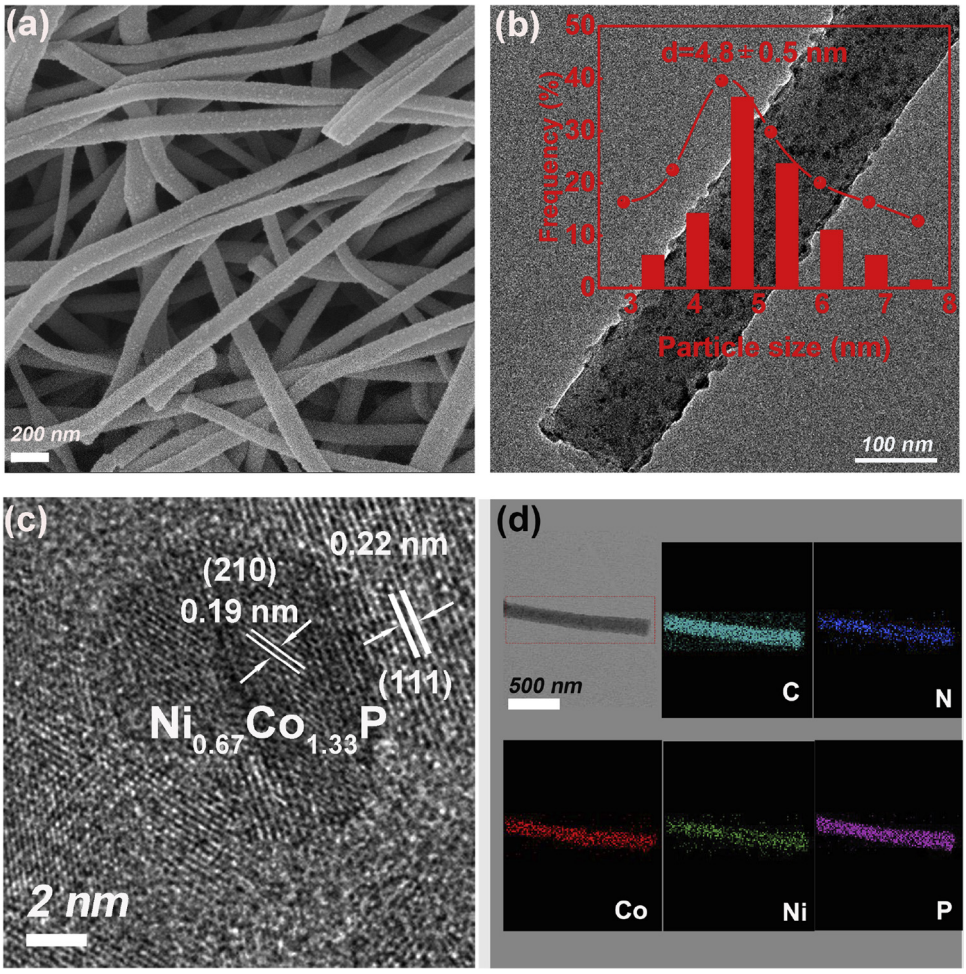

Fig. 2. (a) SEM, (b) TEM and (c) HR-TEM images of the $Ni_{0.67}Co_{1.33}P$/N-C NFs, and (d) HAADF TEM image and the corresponding element mapping of C, N, Ni, P and Co. Inset of b is the particle size distribution of the $Ni_{0.67}Co_{1.33}P$ in NFs.

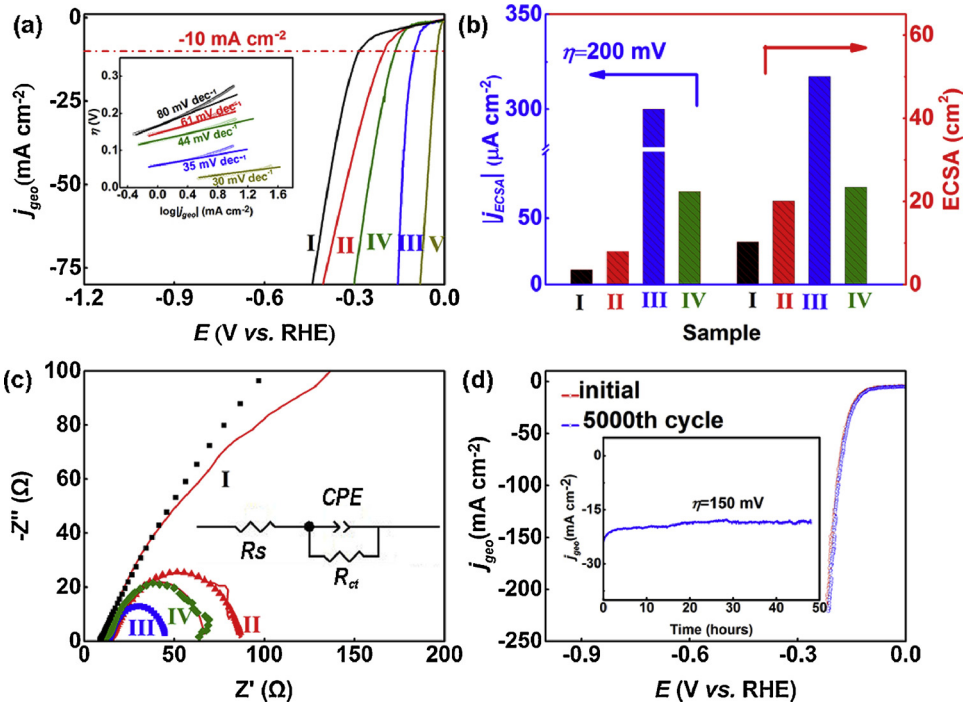

Fig. 3. (a) Polarization curves (inset of a presents the corresponding Tafel plots) and (b) corresponding ECSA and j_{ECSA} of modified GCEs with various $Ni_{2-x}Co_xP$/N-C NFs in 0.5 M H_2SO_4, along with that of commercial 40% Pt/C (I: $Ni_{1.67}Co_{0.33}P$/N-C, II: $Ni_{1.00}Co_{1.00}P$/N-C, III: $Ni_{0.67}Co_{1.33}P$/N-C, IV: $Ni_{0.33}Co_{1.67}P$/N-C, V: 40% Pt/C). (c) Nyquist plots (at η = 150 mV) of $Ni_{2-x}Co_xP$/N-C NFs, and (d) Long-term stability of the $Ni_{0.67}Co_{1.33}P$/N-C NFs in 0.5 M H_2SO_4.

oxygen. And the pyrrolic-N and pyridic-N species are dominant in the samples (Fig. S5), which, possessing planar structures, are beneficial for the electrical conductivity of N-doped carbon [29]. The detectable M–N (M = Ni or Co) species suggests the strong interactions between N-C NFs with TMPs nanoparticles.

Taking the $Ni_{0.67}Co_{1.33}P$/N-C NFs as a model sample, the nanostructure was investigated by SEM and TEM. As shown in Fig. 2a, the $Ni_{0.67}Co_{1.33}P$/N-C NFs are tens microns in length and 150 ~ 200 nm in width. TEM investigation further reveals that small $Ni_{2-x}Co_xP$ nanoparticles evenly distribute in 1D carbon matrix, with an average size of 4.8 ± 0.5 nm (Fig. 2b). Such high dispersity of TMPs stems from the confined growth by *in-situ* formed N-carbon matrix, enabling abundant active-sites for electrocatalysis. Moreover, the visible lattice fringes of 0.20 and 0.22 nm in a high-resolution TEM (HR-TEM) image correspond to the (210) and (111) planes of $Ni_{0.67}Co_{1.33}P$ (Fig. 2c), respectively. In addition, the EDS shows the presence of C, N, P, Ni and Co (Fig. S6), and a Co/Ni molar ratio (1.9) agrees with the formula of the bimetallic $Ni_{0.67}Co_{1.33}P$. The corresponding elemental mapping further confirms the uniform distribution of Co, Ni, P, C and N in a single nanofiber (Fig. 2d).

3.2. HER performance

To investigate HER performance, the $Ni_{2-x}Co_xP$/N-C NFs with varied composition were modified onto GCEs with a loading mass of 0.287 mg cm^{-2}. The commercial Pt/C (40 wt.%) with the benchmarking performance was also measured for a comparison. All the $Ni_{2-x}Co_xP$/N-C NFs outperforms their single-metal counterparts (i.e., Ni-P/N-C and Co-P/N-C, Fig. S7), which indicates the promotion by bimetallic TMPs and is consistent with previous discovery [20]. Fig. 3a presents their polarization curves in 0.5 M H_2SO_4, in term of current density (j_{geo}) in respect to electrode geometrical area. Among the $Ni_{2-x}Co_xP$/N-C NFs, the $Ni_{0.67}Co_{1.33}P$/N-C delivers the best HER activity. It requires an overpotential (η_{10}) as low as 100 mV to reach a j_{geo} of -10 mA cm^{-2}, which is much smaller than that of $Ni_{0.33}Co_{1.67}P$/N-C (165 mV), $Ni_{1.00}Co_{1.00}P$/N-C (200 mV), and $Ni_{1.67}Co_{0.33}P$/N-C (284 mV). This clearly indicates the improved HER activity associated with the optimal composition of bimetallic phosphides, i.e., $Ni_{0.67}Co_{1.33}P$. The excessive (e.g., $Ni_{0.33}Co_{1.67}P$) or insufficient (e.g., $Ni_{1.67}Co_{0.33}P$ and $Ni_{1.00}Co_{1.00}P$) Co in $Ni_{2-x}Co_xP$ leads to relatively lower HER activity.

Accordingly, the Tafel analysis reveals the fast kinetic on the $Ni_{0.67}Co_{1.33}P$/N-C NFs, featuring the low slope of 35 mV dec^{-1} and the low η_{onset} (overpotential referring to the beginning of the linear regime in the Tafel plot) of 48 mV (inset of Fig. 3a). The small Tafel slope indicates a fast increase in H_2 generation rate with applied overpotential [30], consistent with their polarization curves. And it suggests a possible Volmer-Tafel reaction mechanism. By contrast, the higher slopes observed on the $Ni_{0.33}Co_{1.67}P$/N-C, $Ni_{1.00}Co_{1.00}P$/N-C, and $Ni_{1.67}Co_{0.33}P$/N-C indicate the relatively slower kinetics.

To assess the intrinsic activity of TMPs, electrochemical surface area (ECSA) is further taken into account, which however cannot be determined directly because of unclear capacitive behaviour. Alternatively, double-layer capacitance (C_{dl}) proportional to ECSA is utilized, and it is derived from cyclic voltammograms (CVs) with various scan rates in a non-Faradaic window (Figs. S8 and S9). The C_{dl} of $Ni_{0.67}Co_{1.33}P$/N-C NFs (57.2 m F cm^{-2}) is obviously higher than that of $Ni_{1.67}Co_{0.33}P$/N-C NFs (5.9 m F cm^{-2}), $Ni_{1.00}Co_{1.00}P$/N-C NFs (11.4 m F cm^{-2}) and $Ni_{0.33}Co_{1.67}P$/N-C NFs (13.4 m F cm^{-2}), indicating the enriched active surface on the $Ni_{0.67}Co_{1.33}P$/N-C. The ECSA can be further calculated from C_{dl} in respect of an assumed specific capacitance of 40 μF cm_{ECSA}^{-2} on a flat surface [31], showing a maximum at the $Ni_{0.67}Co_{1.33}P$/N-C NFs (Fig. 3b). Moreover, the current densities (j_{ECSA}) normalized by ECSA will present the intrinsic HER activity of various nanocomposites (Fig. S10). Apparently, the highest absolute value of j_{ECSA} on the $Ni_{0.67}Co_{1.33}P$/N-C NFs at η = 200 mV confirms the intrinsically promoted activity (Fig. 3b), which should be ascribed to their engineered electronic configuration on surface.

In addition to catalytic activity, charge transports are also crucial for efficient electrocatalysis. The EIS of $Ni_{2-x}Co_xP$/N-C NFs are measured at η = 150 mV from 10^{-2} to 10^{6} Hz in 0.5 M H_2SO_4 (Fig. 3c). The $Ni_{0.67}Co_{1.33}P$/N-C NFs deliver the lowest resistant charge transfer (R_{ct}), indicating their faster charge-transfer process during H_2 evolution. Meanwhile, the $Ni_{0.67}Co_{1.33}P$/N-C NFs afford satisfied stability for HER in 0.5 M H_2SO_4 (Fig. 3d). The final polarization curves afford negligible degradation in comparison with the initial ones after taking 5000 continuous linear voltammetric cycles. And the chronoamperometry test shows that the $Ni_{0.67}Co_{1.33}P$/N-C NFs can keep a j_{geo} about ~ −20 mA cm^{-2} at η = 150 mV for more than 40 h. Such stability is further indicated by the XRD and TEM investigations taken after cycling test, which clearly identifies the negligible variation in crystallographic structure and morphology (Figs. S11a and S11b). However, the XPS shows slightly oxidized species on catalyst surface (Fig. S11c and S11d), probably owing to the surface alteration involving anions during HER [32].

Analogously, the $Ni_{2-x}Co_xP$/N-C NFs present the consistent trend for HER activity in alkaline and neutral electrolytes, i.e., 1.0 M KOH (Fig. 4a and b) and 1.0 M PBS (Fig. 4d and e). The optimal $Ni_{0.67}Co_{1.33}P$/N-C NFs afford low η_{10} of 130 and 110 mV in 1.0 M KOH and 1.0 M PBS, respectively, outperforming the counterparts with different Co contents. The high absolute values of j_{ECSA} on the $Ni_{0.67}Co_{1.33}P$/N-C NFs in both 1.0 M KOH and 1.0 M PBS (Figs. 4b, e and S12 ~14) strongly indicate the intrinsically improved activity. The merits in HER kinetics and charge-transfer rate are further indicated by their Tafel analysis (inset of Fig. 4a and d) and EIS (Fig. S15). In the examinations by cycling continuously for 5000 cycles and chronoamperometry, the $Ni_{0.67}Co_{1.33}P$/N-C NFs perform well in 1.0 M KOH and 1.0 M PBS (Fig. 4c and f), suggesting the satisfied long-term stability for HER.

Table 1 summarizes the electrocatalytic performance of the $Ni_{2-x}Co_xP$/N-C NFs in 0.5 M H_2SO_4, 1.0 M KOH and 1.0 M PBS. They are highly active for HER in such a wide pH range, highlighting the promise for sustainable water electrolysis in a large variety of scenes [33]. The $Ni_{0.67}Co_{1.33}P$/N-C NFs perform at the high level of recent-reported TMPs electrocatalysts (Table S2). In 0.5 M H_2SO_4, its η_{10} of 100 mV is lower than that of Fe-Co_2P/NCNTs (126 mV) [34], Janus-type Co/CoP nanocrystals (138 mV) [35], Fe_xP@NPC (227 mV) [36] and MoP@PC (153 mV) [37], but higher than that of $WS_{2(1-x)}P_{2x}$ (98 mV) [38] and CoP@NC (78 mV) [39]. And its performance in a neutral electrolyte (η_{10} = 110 mV) outperforms MoP NA/CC (187 mV) [40], Ni_2P@NPCNFs (185 mV) [19], V-CoP/CC (123 mV) [41], etc. In 1.0 M KOH, its excellent activity with a η_{10} of 130 mV is superior to CoP nanowires (147 mV) [42], CoP/C (159 mV) [43], Ni_2P/rGO (142 mV) [44], and Co_2P/WC@NC (180 mV) [45], but interferior to Fe-CoP/Ti (78 mV) [46] and nanoporous CoP_3/Ti (76 mV) [47].

3.3. Theoretical calculation

As summarized in Table 1, the HER activity on $Ni_{2-x}Co_xP$/N-C NFs obviously depends on the composition of bimetallic phosphides. In a wide pH range (0 ~ 14), the $Ni_{0.67}Co_{1.33}P$/N-C NFs deliver obviously higher j_{ECSA} (Fig. S10 and S14) and $j_{0,ECSA}$ (exchange currents normalized on the ECSA, Table 1) in comparison with other $Ni_{2-x}Co_xP$/N-C NFs, which indicates the intrinsically boosted HER on the engineered surface. Herein, DFT calculation is conducted to simulate the varied electronic configuration on active $Ni_{2-x}Co_xP$ (001). As shown in Fig. 5a, the *d*-band center (ε_d) gradually up-shifts from -2.41 to −1.85 eV with increasing Co content (x = 0.33 ~ 1.33). When Co is excessive (x = 1.67), the ε_d slightly downshifts to -1.94 eV. It's indicated that introducing Co into bimetallic $Ni_{2-x}Co_xP$ can bring about more unoccupied *d* orbitals, which is the key to determine the interactions with reaction intermediates. Accordingly, the hydrogen binding energy

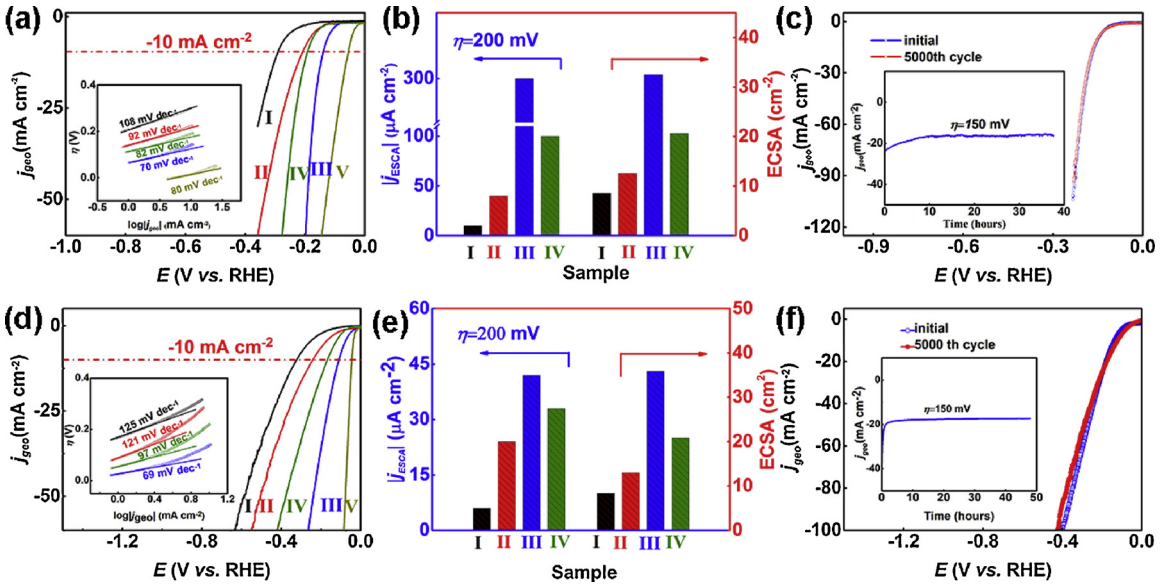

Fig. 4. (a, d) Polarization curves and (b, e) corresponding ECSA and j_{ECSA} at η = 200 mV of phosphide-modified GCEs in (a ~ c) 1.0 M KOH and (d ~ f) 1.0 M PBS, along with that of commercial 40% Pt/C (I: $Ni_{1.67}Co_{0.33}P$/N-C, II: $Ni_{1.00}Co_{1.00}P$/N-C, III: $Ni_{0.67}Co_{1.33}P$/N-C, IV: $Ni_{0.33}Co_{1.67}P$/N-C, V: 40% Pt/C). (c, f) Long-term stability of the $Ni_{0.67}Co_{1.33}P$/N-C NFs in (c) 1.0 M KOH and (f) 1.0 M PBS. Insets of a and d present the Tafel plots.

(HBE) on the above surfaces are calculated. As presented in Fig. 5b, its absolute value increases linearly with the up-shifting ε_d in $Ni_{2-x}Co_xP$, consistent with the observation on metals in previous references [48]. This result clearly verifies the gradually enhanced H-binding on $Ni_{2-x}Co_xP$, although further case study with various H coverage can give more details for the surface behavious during HER [49]. On such $Ni_{2-x}Co_xP$ with increasing Co (x = 0.33 ~ 1.33), the enriched *d*-vacancies and the reduced electrons in M−H anti-bonds are accounting for the variation [50]. Furthermore, the strength of H-binding is quantified by means of the free energy of hydrogen adsorption (ΔG_{H^*}, Fig. 5c). A ΔG_{H^*} value close to 0.0 eV will lead to optimal HER activity [51], e.g., Pt (111) (ΔG_{H^*} = -0.03 eV), because of the balance between the proton reduction and the removal of H* from catalyst surface. Noticeably, the $Ni_{1.67}Co_{0.33}P$ presents a positive ΔG_{H^*} of 0.14 eV, which is far from ideal value zero and suggests the weak H-binding on surface. With increasing Co content, the ΔG_{H^*} approaches to the thermodynamic neutral value, indicating the strengthened H-binding due to enriched d-vacancies. On $Ni_{0.67}Co_{1.33}P$, the ΔG_{H^*} is only 0.06 eV, smaller than that of others $Ni_{2-x}Co_xP$. At this point, the H^+ reduction (Volmer step) and H* desorption (Tafel or Heyrovsky step) are balanced due to the moderated H-binding on catalyst surface. Thereby, the highly active HER is achieved on the $Ni_{0.67}Co_{1.33}P$/N-C NFs.

Meanwhile, the nanostructures of $Ni_{2-x}Co_xP$/N-C NFs also make influences on the electrocatalytic performance. The $j_{0,ECSA}$ on $Ni_{2-x}Co_xP$/N-C NFs represents the varied intrinsic activity at thermodynamical potential, however its difference (Table 1) cannot match the entirely different j_{ECSA} at high overpotentials (e.g., η = 200 mV, Figs. 3b, 4 b and e). In that region, the limitation by mass diffusion becomes obvious on fast HER [52]. As evidenced by N_2 sorption isotherms (Fig. 1b), the $Ni_{0.67}Co_{1.33}P$/N-C NFs possess the largest surface and well-defined mesoporosity (~ 5.6 nm), which will promote the mass transport (electrolytes, H_2 and electrons) at high overpotentials and minimize the diffusion limitation, toward the best HER among $Ni_{2-x}Co_xP$/N-C NFs. Moreover, as $Ni_{0.67}Co_{1.33}P$/N-C nanoparticles are taken for comparision (Fig. S16), their obviously lower HER activity confirms the key role of N-C NFs.

3.4. Electrocatalytic performance of OER and overall water splitting

The OER activity on the $Ni_{2-x}Co_xP$/N-C NFs is further examined in 1.0 M KOH (Fig. 6a). For comparison, the home-made IrO_2/C is also measured, which delivers the benchmarking activity with a η_{10} of ~

Table 1
Summary of the HER activity of $Co_{2-x}Ni_xP$/N-C NFs in acidic, alkaline and neutral electrolytes.

catalyst	electrolyte	η_{10} (mV)	η_{onset} (mV)	Tafel slope (mV dec^{-1})	ECSA (cm^{-2})	C_{dl} (mF cm^{-2}) [a]	$j_{0,\ geo}$ (mA cm^{-2})[b]	$j_{0,\ ECSA}$ (mA cm^{-2})[c]
$Ni_{1.67}Co_{0.33}P$	0.5 M H_2SO_4	284	128	80	10.3	5.9	1.4×10^{-4}	9.5×10^{-7}
$Ni_{1.00}Co_{1.00}P$		200	110	61	20.1	11.4	2.5×10^{-3}	8.7×10^{-6}
$Ni_{0.67}Co_{1.33}P$		100	48	35	50.1	57.2	1.3×10^{-2}	1.8×10^{-5}
$Ni_{0.33}Co_{1.67}P$		165	100	44	23.5	13.4	5.3×10^{-3}	1.6×10^{-5}
$Ni_{1.67}Co_{0.33}P$	1.0 M KOH	289	198	108	8.6	4.9	4.5×10^{-4}	3.6×10^{-6}
$Ni_{1.00}Co_{1.00}P$		206	135	92	12.6	7.2	2.3×10^{-3}	1.3×10^{-5}
$Ni_{0.67}Co_{1.33}P$		130	68	70	32.6	37.2	8.9×10^{-3}	1.9×10^{-5}
$Ni_{0.33}Co_{1.67}P$		190	113	82	20.7	17.7	5.4×10^{-3}	1.8×10^{-5}
$Ni_{1.67}Co_{0.33}P$	1.0 M PBS	326	160	125	8.4	4.8	4.4×10^{-4}	3.6×10^{-6}
$Ni_{1.00}Co_{1.00}P$		241	90	121	13.0	14.8	8.4×10^{-4}	4.5×10^{-6}
$Ni_{0.67}Co_{1.33}P$		110	35	69	35.9	41.1	5.9×10^{-3}	1.1×10^{-5}
$Ni_{1.67}Co_{0.33}P$		163	50	97	20.9	23.8	1.9×10^{-3}	6.4×10^{-6}

[a] Data was calculated from CV results (Figs. S9, S12 and S13).
[b] Exchange-current densities normalized on the geometrical area of GCEs ($j_{0,\ geo}$) were obtained from Tafel curves by using an extrapolation method.
[c] Data of $j_{0,\ ECSA}$ were calculated by assuming that the specific capacitance for a flat surface (1 cm^2) is 40 m F cm^{-2}.

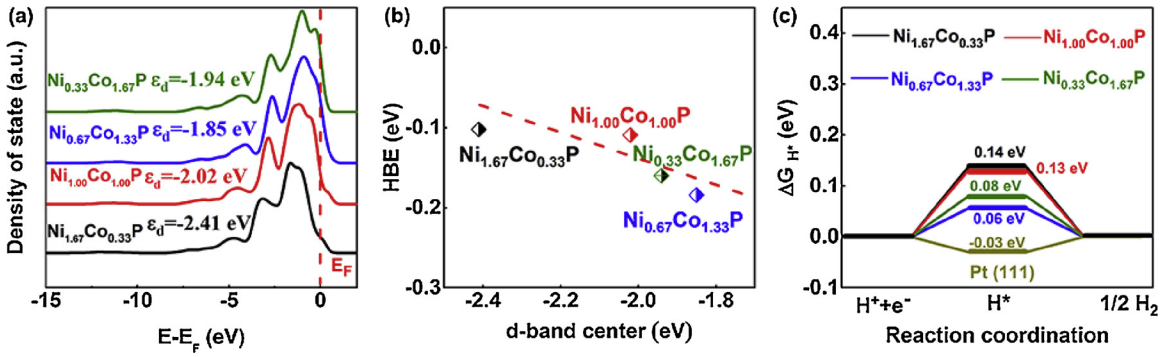

Fig. 5. (a) Density of state, (b) HBE and (c) free energy diagram of HER on the surface of solid-solution alloy $Ni_{2-x}Co_xP$.

240 mV. Remarkably, the $Ni_{0.67}Co_{1.33}P$/N-C NFs afford a η_{10} of 280 mV, lower than that on $Ni_{0.33}Co_{1.67}P$/N-C (370 mV), $Ni_{1.00}Co_{1.00}P$/N-C (393 mV), $Ni_{1.67}Co_{0.33}P$/N-C NFs (462 mV) and the single-metal counterparts (Ni-P/N-C: 580 mV, Co-P/N-C: 516 mV, Fig. S17). Meanwhile, the Tafel plots further verify the promoted kinetics on the $Ni_{0.67}Co_{1.33}P$/N-C NFs (Fig. 5b). They exhibit a Tafel slope of 54 mV dec^{-1}, higher than that of IrO_2/C (41 mV dec^{-1}), but much lower than that of $Ni_{0.33}Co_{1.67}P$/N-C NFs (60 mV dec^{-1}), $Ni_{1.00}Co_{1.00}P$/N-C NFs (101 mV dec^{-1}) and $Ni_{1.67}Co_{0.33}P$/N-C NFs (114 mV dec^{-1}). The fast OER kinetics is suggested on such electronic-modulated phosphides. The enriched *d*-vacancies will enhance the binding with OH* intermediates, resulting in the promoted dissociation and further O_2 generation [6]. In addition, the $Ni_{0.67}Co_{1.33}P$/N-C NFs afford satisfied long-term durability for OER in 1.0 M KOH (Inset of Fig. 6a). Although the $Ni_{0.67}Co_{1.33}P$/N-C NFs well remain their nanostructures and crystallographic texture after OER test (*c.f.* TEM and XRD, Figs. S18a and S18b), its surface suffers visible oxidation due to the highly positive potentials, as indicated by the XPS measurement (Figs. S18c and S18d). Such surface oxidation is important to *in-situ* generate active-sites for efficient OER [53].

Regarding the bi-functionality of the $Ni_{2-x}Co_xP$/N-C NFs for both HER and OER, we construct an electrolyser in a two-electrode configuration for overall water splitting, using the $Ni_{0.67}Co_{1.33}P$/N-C NFs modified GCEs as both cathode and anode electrodes. As displayed in Fig. 6c, the $Ni_{0.67}Co_{1.33}P$ /N-C NFs deliver efficient overall water splitting in 1.0 M KOH, with a catalytic current density of 10 mA cm^{-2} at a cell voltage of 1.56 V. The benchmarking Pt/C-IrO_2/C couple requires a relatively lower voltage (1.50 V) to achieve the same current density. However, the $Ni_{0.67}Co_{1.33}P$/N-C NFs exceed the Pt/C-IrO_2/C at high overpotentials (> 1.75 V), showing its superiority in water

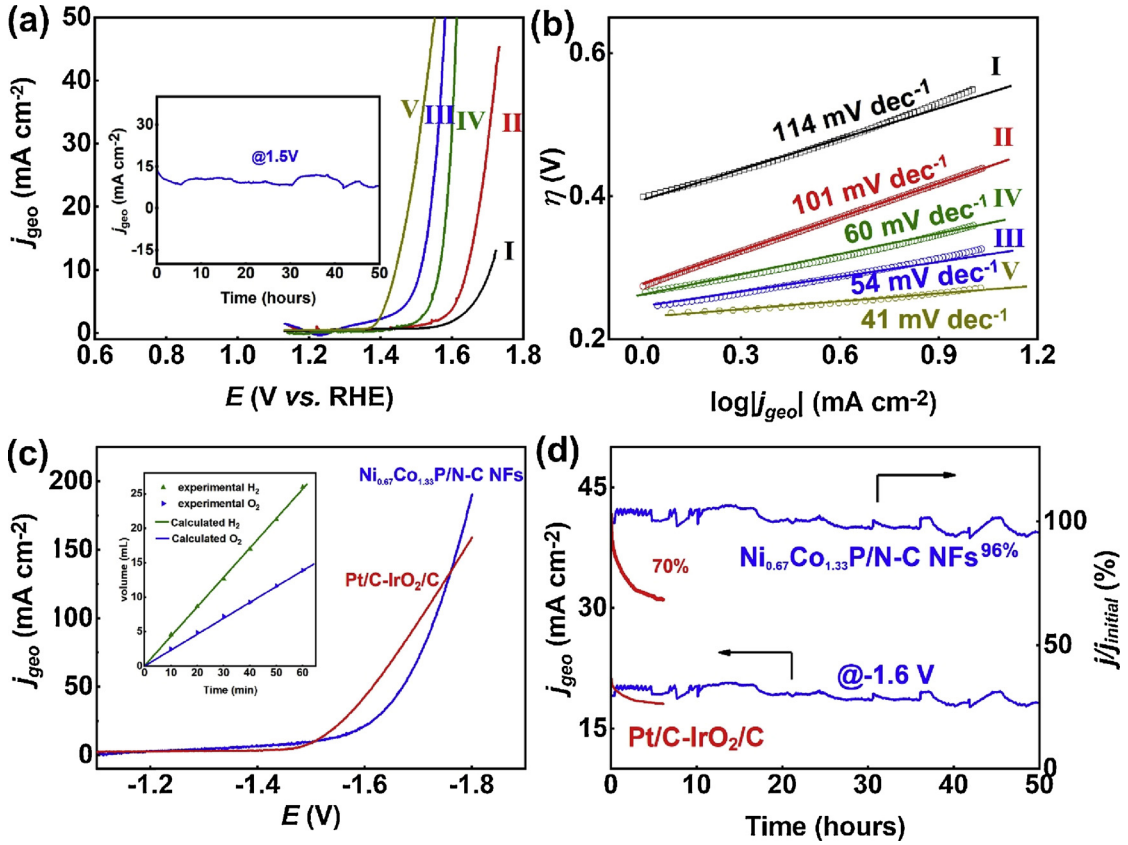

Fig. 6. (a) Polarization curves (b) corresponding Tafel plots for OER on $Ni_{2-x}Co_xP$/N-C NFs modified GCEs in 1.0 M KOH, along with that of commercial 20% IrO_2/C (I: $Ni_{1.67}Co_{0.33}P$/N-C, II: $Ni_{1.00}Co_{1.00}P$/N-C, III: $Ni_{0.67}Co_{1.33}P$/N-C, IV: $Ni_{0.33}Co_{1.67}P$/N-C, V: 20% IrO_2/C). Inset of a depicts the long-term stability of the $Ni_{0.67}Co_{1.33}P$/N-C NFs at 1.5 V vs. RHE. (c) Polarization curves and (d) long-term durability tests (at 1.6 V) of the $Ni_{0.67}Co_{1.33}P$/N-C NFs for overall water splitting in 1.0 M KOH. Inset of c shows the amount of gas theoretically calculated and experimentally measured versus time on the $Ni_{0.67}Co_{1.33}P$/N-C NFs.

splitting at a high rate. Meanwhile, the Faradaic efficiency for both H_2 and O_2 was analyzed (inset of Fig. 6c). The amounts of H_2 and O_2 quantified by gas chromatography are in good accordance with the theoretical values, indicating a high efficiency close to 100% [54]. More importantly, the $Ni_{0.67}Co_{1.33}P$/N-C NFs exhibit an impressive durability operated in 1.0 M KOH. As depicted in Fig. 6d, the j_{geo} of ~20 mA cm^{-2} at 1.6 V shows no obvious decay over 48 h, retaining nearly 96% of initial activity. In sharp contrast, the Pt/C-IrO_2/C couple suffers from obvious deactivation to ~ 70% in a short time (~ 8 h).

4. Conclusions

In summary, we report on bimetallic $Ni_{2-x}Co_xP$/N-C NFs with engineered solid-solution-alloys for the efficient HER in a wide pH range. Via engineering the composition of $Ni_{2-x}Co_xP$, the HER performance is remarkably optimized in acidic, alkaline, and neutral electrolytes, featuring the low η_{10} of 100, 130 and 110 mV, respectively. The varied *d*-band and the consequently enhanced H-binding on $Ni_{2-x}Co_xP$ surface are accounting for the intrinsically improved HER activity. Meanwhile, the ultrafine TMPs integrating with nanoporous and conducting N-doped carbon matrix further promote the mass transport during electrocatalysis, minimizing the limitation of diffusion at high overpotentials. As integrated for overall water splitting in 1.0 M KOH, the optimal $Ni_{0.67}Co_{1.33}P$/N-C NFs further give a high efficiency (1.56 V @ 10 mA cm^{-2}) comparable to the benchmarking IrO_2/C − Pt/C couple, and remarkably better stability. It's envisioned that future work with further control over TMPs facets and their interfacial interactions with carbon matrix would boost the catalytic performance in sustainable energy conversion.

Acknowledgements

This work was financially supported by the National Natural Science Foundation of China (grant no. 21773093 and 21433002), the National Key Research and Development Program of China (2018YFA0209402), the Guangdong Natural Science Funds for Distinguished Young Scholars (grant no. 2015A030306014), and the Science and Technology Program of Guangzhou (grant no. 201707010268). The authors are greatly appreciated to Prof. Dan Li in Jinan University for the kind assistance in DFT simulation.

Appendix A. Supplementary data

Supplementary material related to this article can be found, in the online version, at doi:https://doi.org/10.1016/j.apcatb.2018.11.083.

References

[1] M.S. Dresselhaus, I.L. Thomas, Nature 414 (2001) 332–337.
[2] K. Saravanan, H. Ham, N. Tsubaki, J.W. Bae, Appl. Catal. B: Envrion. 217 (2017) 494–522.
[3] M.S.D. George, W. Crabtree, Michelle V. Buchanan, Phys. Today 57 (2014) 39.
[4] M. Fang, G. Dong, R. Wei, J.C. Ho, Adv. Energy Mater. 7 (2017) 1700559.
[5] C.G. Morales-Guio, L.A. Stern, X. Hu, Chem. Soc. Rev. 43 (2014) 6555–6569.
[6] S. Siracusano, N. Van Dijk, E. Payne-Johnson, V. Baglio, A.S. Arico, Appl. Catal. B Envrion. 164 (2015) 488–495.
[7] Q. Gao, W. Zhang, Z. Shi, L. Yang, Y. Tang, Adv. Mater. (2018), https://doi.org/10.1002/adma.201802880.
[8] S.H. Ahn, B.-S. Lee, I. Choi, S.J. Yoo, H.-J. Kim, E. Cho, D. Henkensmeier, S.W. Nam, S.-K. Kim, J.H. Jang, Appl. Catal. B Envrion. 154 (2014) 197–205.
[9] Y. Wang, B. Kong, D. Zhao, H. Wang, C. Selomulya, Nano Today 15 (2017) 26–55.
[10] Y. Shi, B. Zhang, Chem. Soc. Rev. 45 (2016) 1529–1541.
[11] P.C.K. Vesborg, B. Seger, I. Chorkendorff, J. Phys. Chem. Lett. 6 (2015) 951–957.
[12] W. Cui, Q. Liu, Z. Xing, A.M. Asiri, K.A. Alamry, X. Sun, Appl. Catal. B Envrion. 164 (2015) 144–150.
[13] X. Xiao, C.-T. He, S. Zhao, J. Li, W. Lin, Z. Yuan, Q. Zhang, S. Wang, L. Dai, D. Yu, Energy Environ. Sci. 10 (2017) 893–899.
[14] P. Jiang, Q. Liu, Y. Liang, J. Tian, A.M. Asiri, X. Sun, Angew. Chem. Int. Ed. 53 (2014) 12855–12859.
[15] Q. Liu, J. Tian, W. Cui, P. Jiang, N. Cheng, A.M. Asiri, X. Sun, Angew. Chem. Int. Ed. 53 (2014) 6710–6714.
[16] J. Tian, Q. Liu, N. Cheng, A.M. Asiri, X. Sun, Angew. Chem. Int. Ed. 53 (2014) 9577–9581.
[17] J. Tian, Q. Liu, A.M. Asiri, X. Sun, J. Am. Chem. Soc. 136 (2014) 7587–7590.
[18] X.-D. Wang, Y.-F. Xu, H.-S. Rao, W.-J. Xu, H.-Y. Chen, W.-X. Zhang, D.-B. Kuang, C.-Y. Su, Energy Environ. Sci. 9 (2016) 1468–1475.
[19] M.Q. Wang, C. Ye, H. Liu, M. Xu, S.J. Bao, Angew. Chem. Int. Ed. 57 (2018) 1963–1967.
[20] J. Kibsgaard, C. Tsai, K. Chan, J.D. Benck, J.K. Nørskov, F. Abild-Pedersen, T.F. Jaramillo, Energy Environ. Sci. 8 (2015) 3022–3029.
[21] J. Li, M. Yan, X. Zhou, Z.-Q. Huang, Z. Xia, C.-R. Chang, Y. Ma, Y. Qu, Adv. Funct. Mater. 26 (2016) 6785–6796.
[22] C. Tang, L.F. Gan, R. Zhang, W.B. Lu, X.E. Jiang, A.M. Asir, X.P. Sun, J. Wang, L. Chen, Nano Lett. 16 (2016) 6617–6621.
[23] C. Tang, H.-F. Wang, Q. Zhang, Acc. Chem. Res. 51 (2018) 881–889.
[24] Y.Q. Yang, K. Zhang, H.L. Ling, X. Li, H.C. Chan, L.C. Yang, Q.S. Gao, ACS Catal. 7 (2017) 2357–2366.
[25] P. Xiao, M.A. Sk, L. Thia, X. Ge, R.J. Lim, J.-Y. Wang, K.H. Lim, X. Wang, Energy Environ. Sci. 7 (2014) 2624–2629.
[26] A.-L. Wang, J. Lin, H. Xu, Y.-X. Tong, G.-R. Li, J. Mater. Chem. A 4 (2016) 16992–16999.
[27] X.Q. Ji, R. Zhang, X.F. Shi, A.M. Asiri, B.Z. Zheng, X.P. Sun, Nanoscale 10 (2018) 7941–7945.
[28] J. Chang, Q. Lv, G. Li, J. Ge, C. Liu, W. Xing, Appl. Catal. B Envrion. 204 (2017) 486–496.
[29] H. Lin, W. Zhang, Z. Shi, M. Che, X. Yu, Y. Tang, Q. Gao, ChemSusChem 10 (2017) 2597–2604.
[30] Q. Mo, N. Chen, M. Deng, L. Yang, Q. Gao, ACS Appl. Mater. Interfaces 9 (2017) 37721–37730.
[31] C. Zhang, Y. Huang, Y. Yu, J. Zhang, S. Zhuo, B. Zhang, Chem. Sci. 8 (2017) 2769–2775.
[32] F.H. Saadi, A.I. Carim, W.S. Drisdell, S. Gul, J.H. Baricuatro, J. Yano, M.P. Soriaga, N.S. Lewis, J. Am. Chem. Soc. 139 (2017) 12927–12930.
[33] S. Gupta, N. Patel, R. Fernandes, R. Kadrekar, A. Dashora, A.K. Yadav, D. Bhattacharyya, S.N. Jha, A. Miotello, D.C. Kothari, Appl. Catal. B Envrion. 192 (2016) 126–133.
[34] Y. Pan, Y. Liu, Y. Lin, C. Liu, ACS Appl. Mater. Interfaces 8 (2016) 13890–13901.
[35] H. Wang, S. Min, Q. Wang, D. Li, G. Casillas, C. Ma, Y. Li, Z. Liu, L.J. Li, J. Yuan, M. Antonietti, T. Wu, ACS Nano 11 (2017) 4358–4364.
[36] Y. Cheng, J. Guo, Y. Huang, Z. Liao, Z. Xiang, Nano Energy 35 (2017) 115–120.
[37] J. Yang, F. Zhang, X. Wang, D. He, G. Wu, Q. Yang, X. Hong, Y. Wu, Y. Li, Angew. Chem. Int. Ed. 55 (2016) 12854–12858.
[38] T.A. Shifa, F.M. Wang, K.L. Liu, Z.Z. Cheng, K. Xu, Z.X. Wang, X.Y. Zhan, C. Jiang, J. He, Small 13 (2017) 1603706.
[39] F. Yang, Y. Chen, G. Cheng, S. Chen, W. Luo, ACS Catal. 7 (2017) 3824–3831.
[40] Z. Pu, S. Wei, Z. Chen, S. Mu, Appl. Catal. B Envrion. 196 (2016) 193–198.
[41] X. Xiao, L. Tao, M. Li, X. Lv, D. Huang, X. Jiang, H. Pan, M. Wang, Y. Shen, Chem. Sci. 9 (2018) 1970–1975.
[42] M. Zhang, S. Ci, H. Li, P. Cai, H. Xu, Z. Wen, Int. J. Hydrogen Energy 42 (2017) 29080–29090.
[43] B. Luo, T. Huang, Y. Zhu, D. Wang, J. Energy Chem. 26 (2017) 1147–1152.
[44] L. Yan, H. Jiang, Y. Xing, Y. Wang, D. Liu, X. Gu, P. Dai, L. Li, X. Zhao, J. Mater. Chem. A 6 (2018) 1682–1691.
[45] Y. Gao, Z. Lang, F. Yu, H. Tan, G. Yan, Y. Wang, Y. Ma, Y. Li, ChemSusChem 11 (2018) 1082–1091.
[46] C. Tang, R. Zhang, W.B. Lu, L.B. He, X. Jiang, A.M. Asiri, X.P. Sun, Adv. Mater. 29 (2017) 1602441.
[47] Y.Y. Ji, L. Yang, X. Ren, G.W. Cui, X.L. Xiong, X.P. Sun, ACS Sustain. Chem. Eng. 6 (2018) 11186–11189.
[48] J.R. Kitchin, J.K. Nørskov, M.A. Barteau, J.G. Chen, Catal. Today 105 (2005) 66–73.
[49] R. Michalsky, Y.-J. Zhang, A.A. Peterson, ACS Catal. 4 (2014) 1274–1278.
[50] B. Hammer, J.K. Norskov, Nature 376 (1995) 238.
[51] X. Ji, B. Liu, X. Ren, X. Shi, A.M. Asiri, X. Sun, ACS Sustain. Chem. Eng. 6 (2018) 4499–4503.
[52] D. Escalera-Lopez, Y. Niu, S.J. Park, M. Isaacs, K. Wilson, R.E. Palmer, N.V. Rees, Appl. Catal. B Envrion. 235 (2018) 84–91.
[53] Y. Yang, W. Zhang, Y. Xiao, Z. Shi, X. Cao, Y. Tang, Q. Gao, Appl. Catal. B Envrion. 242 (2019) 132–139.
[54] T.T. Liu, L.S. Xie, J.H. Yang, R.M. Kong, G. Du, A.M. Asiri, X.P. Sun, L. Chen, ChemElectroChem 4 (2017) 1840–1845.